2023

Sub-monthly prediction of harmful algal blooms based on automated cell imaging

Vitul Agarwal
University of Rhode Island

Jonathan Chávez-Casillas
University of Rhode Island, jchavezc@uri.edu

Colleen B. Mouw
University of Rhode Island, cmouw@uri.edu

Citation/Publisher Attribution

Agarwal, V., Chávez-Casillas, J., & Mouw, C. B. (2023). Sub-monthly prediction of harmful algal blooms based on automated cell imaging. *Harmful Algae, 122*, 102386. https://doi.org/10.1016/j.hal.2023.102386
Available at: https://doi.org/10.1016/j.hal.2023.102386

Sub-monthly prediction of harmful algal blooms based on automated cell imaging

Vitul Agarwal[1], Jonathan Chávez-Casillas[2] and Colleen B. Mouw[1]

[1]Graduate School of Oceanography, University of Rhode Island, Narragansett, USA

[2]Department of Mathematics and Applied Mathematical Sciences, University of Rhode Island, Kingston, USA

Running title: Timescales of HAB prediction

Emails: vitulagarwal@uri.edu; jchavezc@uri.edu; cmouw@uri.edu

ORCID IDs

Vitul Agarwal (0000-0002-1523-9044)

Jonathan Chávez-Casillas (0000-0002-8494-7538)

Colleen B. Mouw (0000-0003-2516-1882)

Authors' Contributions and Conflict of Interest

All authors helped prepare the manuscript and approved the final version. The authors declare no competing interests.

Data availability statement

All data and code required for the analysis will be made publicly available upon publication.

Abstract

Harmful algal blooms (HABs) are an increasing threat to global fisheries and human health. The mitigation of HABs requires management strategies to successfully forecast the abundance and distribution of harmful algal taxa. In this study, we attempt to characterize the dynamics of 2 phytoplankton genera (*Pseudo-nitzschia spp.* and *Dinophysis spp.*) in Narragansett Bay, Rhode Island, using empirical dynamic modeling. We utilize a high-resolution Imaging FlowCytobot dataset to generate a daily-resolution time series of phytoplankton images and then characterize the sub-monthly (1-30 days) timescales of univariate and multivariate prediction skill for each taxon. Our results suggest that univariate predictability is low overall, different for each taxon and does not significantly vary over sub-monthly timescales. For all univariate predictions, models can rely on the inherent autocorrelation within each time series. When we incorporated multivariate data based on quantifiable image features, we found that predictability increased for both taxa and that this increase was apparent on timescales >7 days. *Pseudo-nitzschia spp.* has distinctive predictive dynamics that occur on timescales of around 16 and 25 days. Similarly, *Dinophysis spp.* is most predictable on timescales of 25 days. The timescales of prediction for *Pseudo-nitzschia spp.* and *Dinophysis spp.* could be tied to environmental drivers such as tidal cycles, water temperature, wind speed, community biomass, salinity, and pH in Narragansett Bay. For most drivers, there were consistent effects between the environmental variables and the phytoplankton taxon. Our analysis displays the potential of utilizing data from automated cell imagers to forecast and monitor harmful algal blooms.

Keywords: Imaging FlowCytobot (IFCB); empirical dynamic modeling (EDM); Narragansett Bay; phytoplankton population dynamics; ecological forecasting; Pseudo-nitzschia; Dinophysis

Introduction

Harmful algal blooms (HABs) are anomalous increases in phytoplankton abundance, biomass, or distribution that can negatively affect marine ecosystems and public health (Fleming et al. 2011; Berdalet et al. 2016; Karlson et al. 2021). The rising frequency of such events in the past few decades is of increasing global concern (Xiao et al. 2019; Gobler 2020). Some estimates of economic damage due to HABs exceed hundreds of millions of dollars (Anderson et al. 2000), often due to fisheries closures (Brown et al. 2020; Sakamoto et al. 2021), disruption to tourism (Smith et al. 2019; Béchard 2020) and damage to human health (Grattan et al. 2016; Kouakou and Poder 2019). Consequently, the successful prediction and mitigation of HABs is a research priority for state and national governments worldwide (Park et al. 2013; Brooks et al. 2016).

HAB predictions often require large amounts of data from various sources and sophisticated modeling techniques (Franks 2018; Ralston and Moore 2020), as well as detailed information on local and regional oceanographic features (Anderson et al. 2010; Dippner et al. 2011; Lapucci et al. 2022). Due to the requirement of high resolution and consistent data, monitoring programs are implementing automated systems (Babin et al. 2005; Jochens et al. 2010) with extensively trained algorithms (Sosik and Olson 2007; Ellen et al. 2019; Orenstein et al. 2020) that can identify and alert local officials of the presence, abundance and risk of HAB development. The rapid deployment of such systems has greatly expanded the ability to detect HABs; however, less is known about the utility of imaging data for HAB prediction models.

In this study, we explored the use of phytoplankton imaging data for HAB predictions in Narragansett Bay, Rhode Island (NBay). Narragansett Bay is a shallow coastal marine estuary of great cultural, historical, and economic importance to local communities (Herndon and Sekatau 1997; Dalton et al. 2010; Nixon and Fulweiler 2012). Coastal marine estuaries are highly dynamic

environments that are subject to seasonality (Carstensen et al. 2015), the influence of both freshwater and seawater sources (Pilson 1985), large-scale climate phenomena (Scavia et al. 2002), and anthropogenic inputs of nutrients (Cundell 1973; Goldberg et al. 1977). Within the past decade, toxic harmful algal blooms have led to fisheries closures in Narragansett Bay (Bates et al. 2018) and motivated extensive research into the potential environmental drivers and species composition (Sterling et al. 2022) of the relevant bloom-causing phytoplankton genera. Of particular importance in this area are *Pseudo-nitzschia spp.* and *Dinophysis spp.* due to their potential toxicity and relevance for local fishery disruption.

Natural phytoplankton populations are variable from daily, seasonal to decadal timescales (Chavez et al. 2003; Barton et al. 2016; Blauw et al. 2018). High variability in natural phytoplankton populations is characteristic of non-linear and chaotic dynamics (Ascioti et al. 1993; Smayda 1998). In this paper, we used empirical dynamic modeling (EDM) to predict the abundance of *Pseudo-nitzschia spp.* and *Dinophysis spp.* in Narragansett Bay, Rhode Island. These genera were selected for a couple of reasons: their role in local harmful algal blooms and the availability of a dynamic, regular time series that would allow for the use of data-driven analyses. EDM is a non-parametric framework that can avoid the pitfalls of typical statistical modeling by relying on data-driven attractor reconstruction (Perretti et al. 2013; Chang et al. 2017).

Our goal was to characterize the sub-monthly univariate and multivariate prediction timescales of *Pseudo-nitzschia spp.* and *Dinophysis spp.* utilizing a high temporal resolution dataset generated with an Imaging FlowCytobot (Olson and Sosik 2007). Automated instruments such as the Imaging FlowCytobot generate datasets of phytoplankton images and many associated features (i.e. image texture, contrast, object size etc.). Specifically, we aim to answer (1) How predictable are the harmful algal target species? (2) How does this predictability vary with time?

and (3) Which image features best describe the dynamics of the taxa? Once we identified the important timescales, we also linked specific environmental drivers to the dynamics of the phytoplankton populations. Our study did not attempt to offer detailed mechanistic explanations of observed phenomena, nor develop tools that might model the growth and termination of harmful algal blooms, but instead, it focused on identifying the potential of imaging data in prediction models. By identifying the relevant dynamical timescales of harmful algal blooms, we also hoped to provide local and regional management with a critical timeframe of action for the development of environmental policy. Our underlying assumption was that the predictability of *Pseudo-nitzschia spp.* and *Dinophysis spp.* in Narragansett Bay had distinct timescales that varied in response to environmental drivers and intrinsic population dynamics.

Materials and Methods

Automated cell imaging

All the time series used in this study were collected by deploying an Imaging FlowCytobot (IFCB) in Narragansett Bay, Rhode Island. The IFCB is an automated, flow-through imaging system that captures images of the extant phytoplankton community in seawater. The system has a maximum size limit of 150µm and works by drawing water at approximately 1m under the surface at low tide. As our IFCB was deployed at the end of a pier (41.492ºN, 71.419ºW), the actual sampling depth varied with the tidal cycle. Images can be observed in real-time using the IFCB dashboard (http://ifcb-dashboard.gso.uri.edu/).

The IFCB samples approximately every 20 minutes depending on the number of cells within a given sample. We used daily aggregated IFCB data from 14th June 2017 to 20th October

2021, barring gaps in the time series due to equipment malfunction or maintenance. Our data span 1590 days of observation with 518 days of missing data. For prediction tasks, all missing data points were approximated using 30-day exponential moving averages (EMA) computed by the R package "imputeTS" (Moritz and Bartz-Beielstein 2017). We used daily aggregated data, instead of other shorter timescales (such as 1-hr or 12-hr) for three broad reasons: the influence of high time series autocorrelation, irregular gaps in data collection, and, to strike a balance between computational costs and expected analytical benefit.

A machine-learning approach was used to identify and classify the phytoplankton taxa from a subset of annotated images (Sosik and Olson 2007). All obtained images classified as *Pseudo-nitzschia spp*. and *Dinophysis spp*. were counted and reported as a concentration based on the average sampling volume for each day ($images\ mL^{-1}$). Higher concentrations of images act as a proxy of higher abundance in the natural environment and lower concentrations of images show that the taxon is rare/absent. To test the general ability to use image concentration as a proxy for phytoplankton abundance, we visually compared our image concentration time series to a long-term weekly monitoring site located approximately 12km north of our IFCB location (https://web.uri.edu/gso/research/plankton/). Figure S1 highlights that our IFCB image concentration agreed with the general pattern of *Pseudo-nitzschia spp.* abundance in Narragansett Bay (as determined by microscopy counts) over the duration of our time series.

We evaluated the classifier's performance for sensitivity and precision with a manually annotated library of images. Table 1 reports the performance of the classifier for *Pseudo-nitzschia spp*. and *Dinophysis spp*.

$$Sensitivity = \frac{TP}{TP + FN}$$

$$Precision = \frac{TP}{TP + FP}$$

where TP, FP and FN were the number of true positive, false positive, and false negative images.

Table 1: Sensitivity and precision of the automatic classifier for each of the phytoplankton classes.

	Sensitivity	**Precision**
Pseudo-nitzschia spp. (N=626)	0.85	0.94
Dinophysis spp. (N=412)	0.95	0.96

236 image features are automatically estimated for each IFCB image (Sosik and Olson 2007, https://github.com/hsosik/ifcb-analysis/wiki). We selected 20 features for further analysis based on their relevance to phytoplankton morphology and ecology (Sonnet et al. 2022). The average daily values for the image features, scaled by the average sampling volume for each day, formed a multi-dimensional time series for each taxon. Table 2 lists all the features and their units.

Table 2: List of all image features used in this study and their units.

Feature	Units
area	$pixels^2$
biovolume	$pixels^3$
major axis	$pixels$
minor axis	$pixels$
perimeter	$pixels$
orientation	$degrees$
eccentricity	-
solidity	-
texture uniformity	-
texture smoothness	-
texture gray	-
texture entropy	-
texture contrast	-
h90	$pixels$
h180	$pixels$
hflip	$pixels$
extent	$pixels$
equivalent diameter	$pixels$
convex area	$pixels^2$
convex perimeter	$pixels$

Environmental data

We compiled data from various monitoring programs located in and around Narragansett Bay. Daily averages of water temperature ($°C$), salinity (ppt), chlorophyll ($\mu g\ L^{-1}$), and pH were requested from the Narragansett Bay Fixed Site Monitoring Network (NBFSMN, personal communication: Heather Stoffel). These measurements were co-located with the Imaging FlowCytobot. Daily averages of wind speed ($m\ s^{-1}$) were drawn from the Kingston weather station (41.49ºN 71.54ºW; U.S. Climate Reference Network; https://www1.ncdc.noaa.gov/pub/data/uscrn/products/subhourly01/). Daily averages of tidal height (Mean Sea Level; m) were calculated from measurements at the NOAA Quonset Point Buoy (41° 35.2 N, 71° 24.6 W; #8454049; https://tidesandcurrents.noaa.gov/). Additional environmental data, such as ambient nutrient concentrations, were not available at the same temporal scale as the imaging data used in the study.

Univariate predictions

We used empirical dynamic modeling (EDM) to make univariate predictions for the time series of each harmful algae. Every time series was normalized (i.e. subtracting the mean value of the time series and dividing by the standard deviation of the time series) before the application of EDM. Specifically, we relied on simplex projection (Sugihara and May 1990) with a consistent embedding dimension of 4 and leave-one-out cross validation. This means that the univariate attractor of a time series was embedded in a 4-dimensional space using the original times series and successive lags of the same time series. Each point is described by $(x_t, x_{t-1}, x_{t-2}, x_{t-3})$ where x_t is the value of x at time point t, x_{t-1} is its value at time $t-1$, and so on. The embedding

dimension was set at 4 to prevent overfitting and maximize the utilization of our daily-scale time series data. Figure S2 shows how varying the embedding dimension affects the predictability of each taxon with fixed prediction intervals of 1, 7, 14 and 28 days. An embedding dimension of 4 allowed for reasonable descriptions across all timescales for both taxa, with a lower risk of overfitting our models to potentially noisy dynamics. The model creation and prediction sets were randomly selected from the entire time series in intervals of 250 days. After bootstrapping 200 samples for each taxon, we generated a mean prediction and 95% confidence intervals $(1.96 \times SE)$. By randomizing the selection of model and prediction libraries, we tried to account for the effects of imputed data into the time series, as well as avoid the effects of possible non-stationarity over the 1590 days of data.

We tested the predictability of each taxon for timescales of 1 to 30 days. Predictability was described by ρ_{model}, the Pearson correlation coefficient, between the observed and the predicted values after attractor reconstruction. To account for inherent autocorrelation within each time series, we subtracted the absolute value of the autocorrelation coefficient at each timescale of prediction. The effective value of predictability was reported as $\Delta\rho$, which is the arithmetic difference of the univariate predictability ρ_{model} and the autocorrelation coefficient ρ_{auto}. Therefore, $\Delta\rho$ quantifies the ability of our model to predict dynamics beyond autocorrelation across a range of sub-monthly timescales. Due to the short timescales of prediction in this study (<30 days), our dataset of 1590 days provided reasonable coverage of all possible sub-monthly dynamics for these harmful algal taxa.

Multiview Embeddings (MVE)

Multiview embeddings are an effective technique for increasing predictability and drawing out information from multiple related time series (Ye and Sugihara 2016). We used MVE to utilize the associated dataset of image features collected by the IFCB. Once more, the embedding dimension was set to 4 for all taxa and the entire time series was used for model and prediction libraries. We relied on leave-one-out cross-validation instead of separate model and prediction libraries.

Each multivariate attractor was created by randomly selecting 3 normalized time series of features and the original time series of image concentration ($images\ mL^{-1}$). Our goal was to predict the proxy abundance of each taxon by leveraging information stored in the image features. Predictability was evaluated for timescales of 1-30 days and reported as $\Delta\rho$ (model predictability beyond autocorrelation), RMSE (root-mean-square error) and MAE (mean absolute error). We considered 500 trials of image feature combinations and reported predictability as the arithmetic mean with 95% confidence intervals ($1.96 \times SE$).

For the best multivariate models (top 5% in terms of ρ_{model}), we reported the frequency of appearance for each image feature as a proportion. A proportion of 0 implies that the feature did not show up in the best multivariate models while a proportion of 1 implies that it was always present. Based on the frequency of appearance, we could deduce the contribution of each feature in improving the overall predictability of the phytoplankton species.

Convergent Cross Mapping (CCM)

Once we identified any relevant timescales of prediction, we wanted to understand whether there was a link between the abundance of harmful algal taxa and relevant environmental drivers. We used convergent cross mapping (CCM; Sugihara et al. 2012) to infer causation between the environmental dataset and image concentration ($images\ mL^{-1}$). Embedding dimensions were optimized (i.e. selecting the embedding dimension that provides the highest prediction skill ρ) to each environmental variable (up to a maximum of 7 to prevent overfitting) and library sizes ranged from 100 - 1400 in intervals of 100 days. There were 20 samples each for every library size and the time to prediction ranged from 1-30 days. We tested whether we could infer causation by predicting the values of past environmental variables from the abundance of the harmful algal taxa. Predictability was quantified by the cross-map prediction skill (ρ), where higher values indicate better predictions. Convergence was estimated using three tests – (1) Mann-Kendall trend test for ρ with increasing library size, (2) a Student's t-test for the ρ distributions at the maximum and minimum library size and (3) by validating that the prediction skill ρ at the maximum library size was greater than the Pearson correlation coefficient between image concentration and the environmental time series. Only the predictions which satisfied all conditions and were significant for both the Mann-Kendall and the Student's t-test (p-value < 0.05) were deemed convergent. If any of the tests failed, then the causal effect of the environmental variable on the phytoplankton taxa was deemed to be unresolved at those specific timescales. Cross-map prediction skill (ρ) was normalized to the embedding dimension by averaging ρ across prediction horizons (Saberski et al. 2021).

Software

All the analyses were conducted in R (R Core Team 2021). For plotting and data visualization, we used the R packages "ggplot2" (Wickham 2016) and "cowplot" (Wilke 2020). EDM was applied using pre-built functions in the R package "rEDM" (Park et al. 2022). Additionally, the R package "Kendall" (McLeod 2022) was used to conduct some statistical tests.

Results

Both *Pseudo-nitzschia spp.* and *Dinophysis spp.* in Narragansett Bay showed intermittent periods of high and low abundance in Narragansett Bay. The IFCB captured such bloom dynamics using the concentration of identified images of both taxa (Figure 1; left column). When evaluated for the autocorrelation inherent within each time series, both *Pseudo-nitzschia spp.* and *Dinophysis spp.* had decreasing autocorrelation with time (Figure 1; right column). The decrease was more rapid for *Pseudo-nitzschia spp.* (ACF < 0.25 within 7 days), whereas *Dinophysis spp.* showed a more gradual decrease over the entire 30 days.

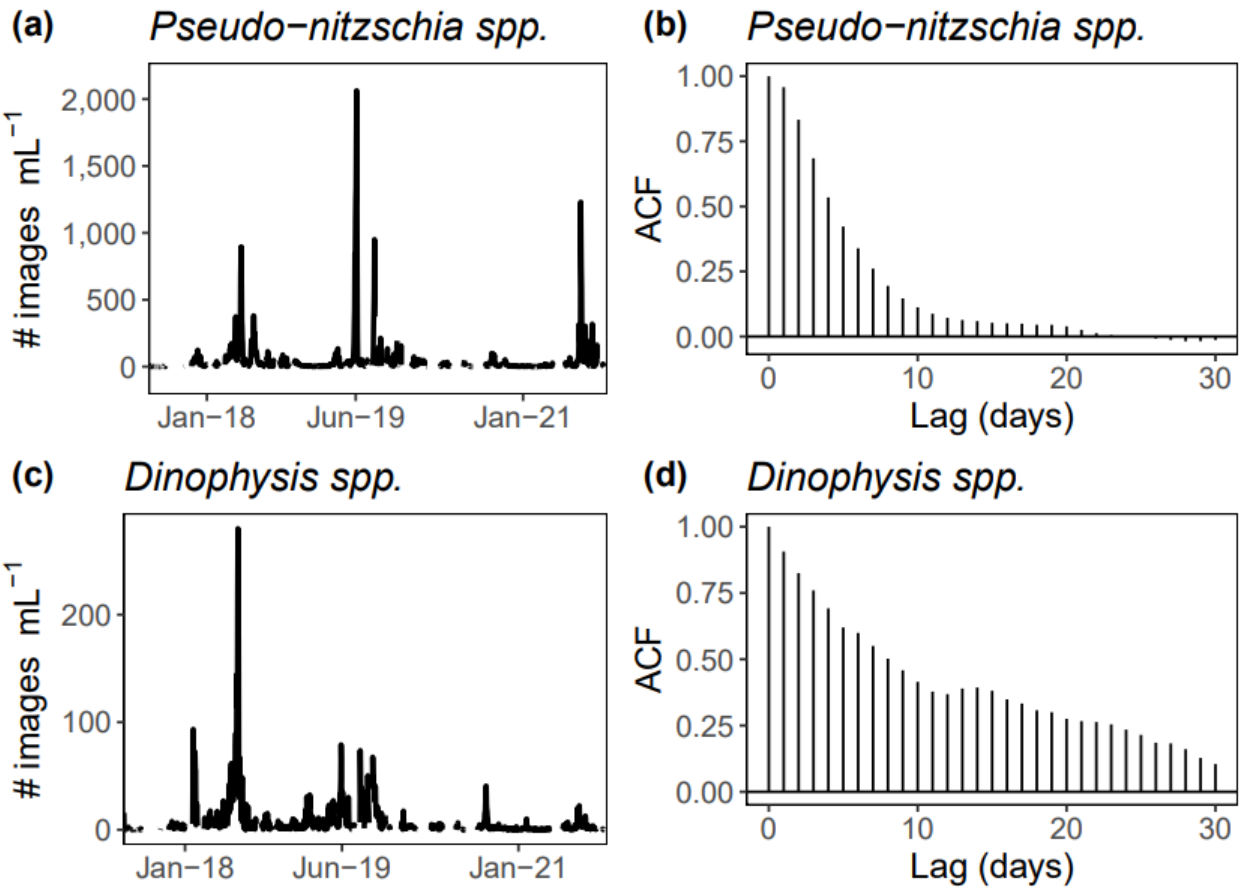

Figure 1: Time series of 2 harmful algal bloom-forming taxa in Narragansett Bay, Rhode Island (left column) and their associated autocorrelation functions (ACF; right column). Relative abundance is estimated from the number of unique images taken by the IFCB and classified as (a) *Pseudo-nitzschia spp.* and (c) *Dinophysis spp.* Autocorrelation decreases with time and varies depending on the dynamics of each specific taxon.

The univariate predictability of both time series ($\Delta\rho$) was low overall and did not greatly change over a prediction horizon of 30 days. The univariate predictability of *Dinophysis spp.* indicated some promise of the model over autocorrelation on horizons of >28 days, whereas the results for *Pseudo-nitzschia spp.* indicated that there is little to no predictability inherent within the time series beyond autocorrelation across all sub-monthly timescales.

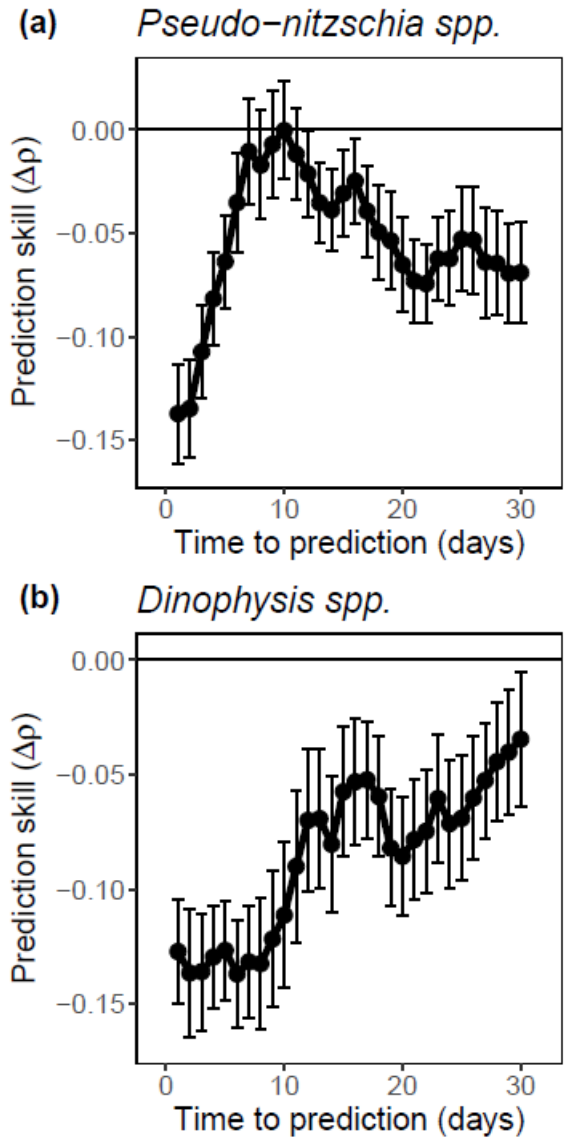

Figure 2: Univariate prediction skill **($\Delta\rho$)** of the time series of (a) *Pseudo-nitzschia spp.* and (b) *Dinophysis spp.* over a prediction horizon of 1-30 days. Model predictions (ρ_{model}) were calculated from 200 random libraries of 250 days each and the results were reported as an arithmetic mean with 95% confidence intervals ($\pm 1.96 \times S.E.$). $\Delta\rho$ was calculated by subtracting the autocorrelation coefficient at each prediction horizon.

Multivariate prediction skill ($\Delta\rho$), calculated using the time series of image abundance and 3 associated image features, was much higher than the univariate prediction skill for both *Pseudo-nitzschia spp.* and *Dinophysis spp.* Using the original time series with only 3 image features at a

288 time (multivariate embedding dimension = 4) allowed for direct comparisons to the univariate
289 prediction skill. The predictability of *Pseudo-nitzschia spp.* had distinctive cycles with peaks every
290 16 and 25 days. An increase in model predictability over autocorrelation was most prominent after
291 a 3-day prediction horizon. The predictability of *Dinophysis spp.* was also higher than inherent
292 autocorrelation after a 6-day prediction horizon. *Dinophysis spp*. had multiple peaks in $\Delta\rho$ at
293 prediction horizons of 10-20 days, with a distinct peak at 25 days. The RMSE of the predictions
294 also showed a distinct drop around the 25-day mark.

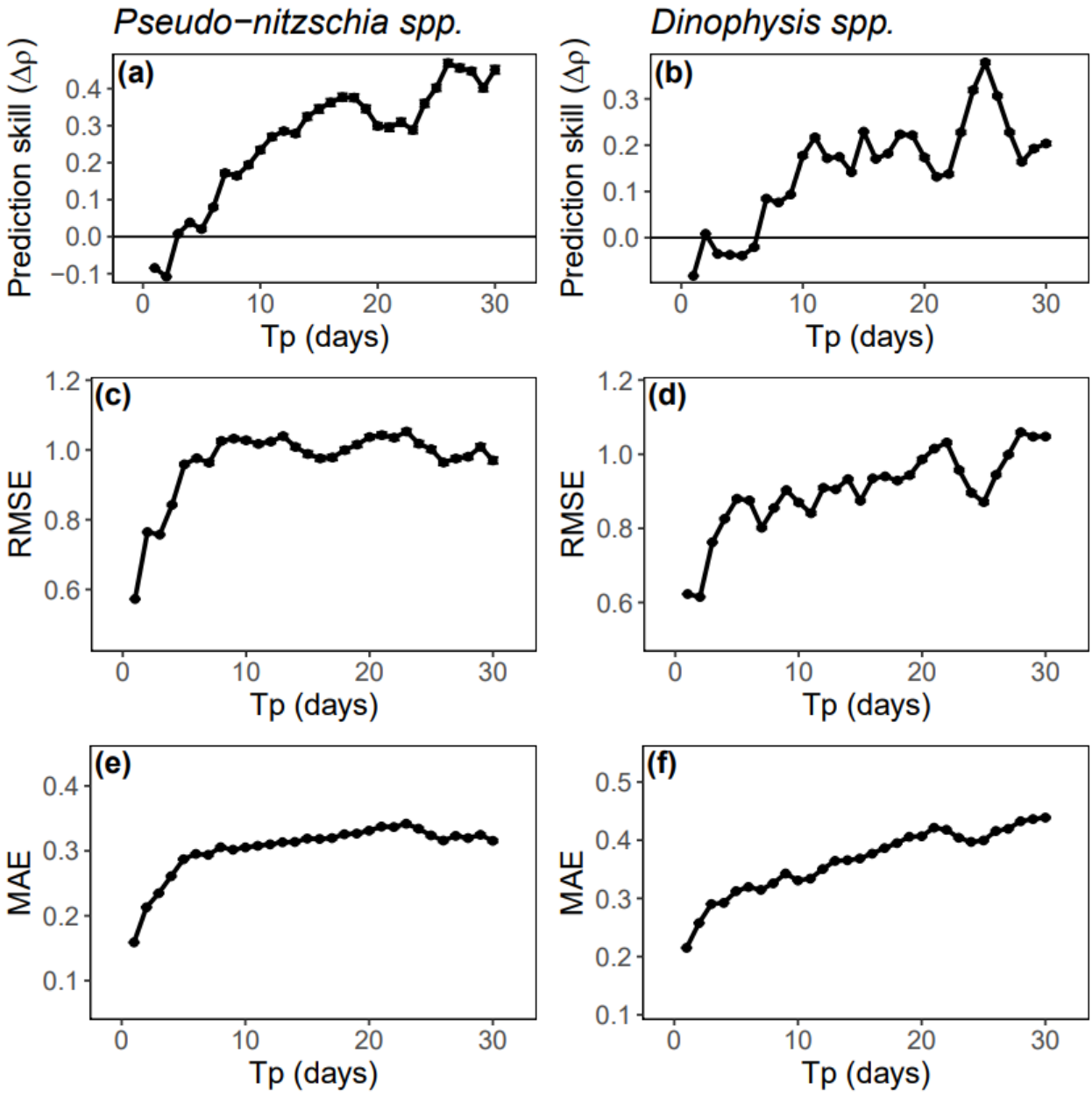

Figure 3: Multivariate prediction skill of the time series of *Pseudo-nitzschia spp.* (left column) and *Dinophysis spp.* (right column) over a prediction horizon of 1-30 days. (a) and (c) report prediction skill **($\Delta\rho$)** calculated by subtracting the autocorrelation coefficient at each prediction horizon, (b) and (d) report prediction error as the root-mean-squared-error (RMSE), (e) and (f) report prediction error as the mean-absolute-error (MAE). Model results were calculated from 500 embeddings of phytoplankton abundance and 3 unique image features. The results were reported as an arithmetic mean with 95% confidence intervals ($\pm 1.96 \times S.E.$).

304 Without accounting for autocorrelation, some multivariate models for both *Pseudo-*
305 *nitzschia spp.* and *Dinophysis spp*. reached prediction skills of 0.70 and greater (Figure 4&5; left).
306 The top 5% of these multivariate models had a fairly uniform distribution of image features, with
307 some clear exceptions. The time series of biovolume and orientation prominently appeared in the
308 top multivariate models for *Pseudo-nitzschia spp.*, whereas the time series of solidity and hflip
309 were present but in a distinctly lower frequency compared to the other features. For *Dinophysis*
310 *spp.*, the time series of biovolume, texture gray and orientation were prominently present in the
311 top multivariate models.

312

313

314

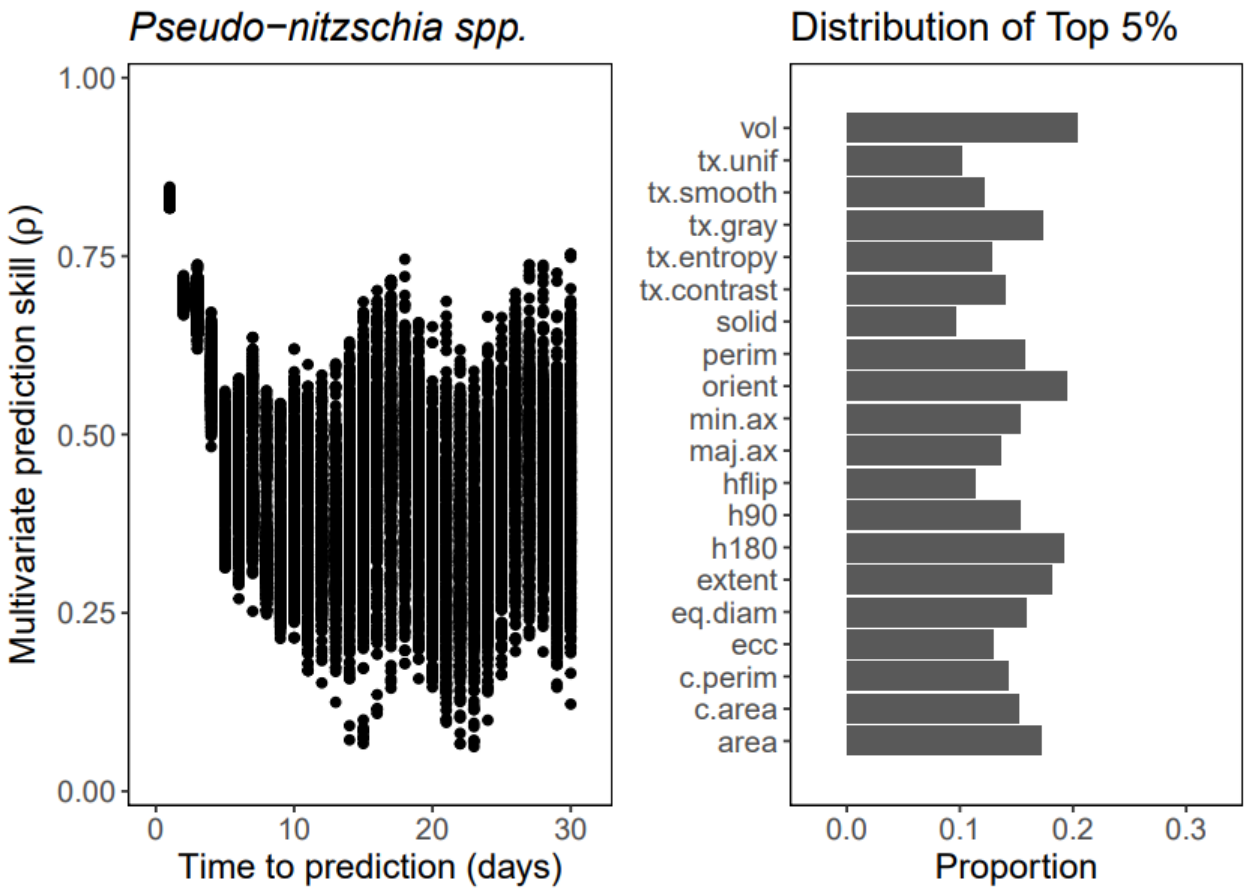

315

316 **Figure 4:** Multivariate prediction skill of the time series of *Pseudo-nitzschia spp.* (ρ; left) over a
317 prediction horizon of 1-30 days. Prediction skill **(ρ)** refers to the Pearson correlation coefficient
318 between model predictions and actual observations. Model results were calculated from 1000
319 embeddings of phytoplankton abundance and 3 unique image features. Each point is the outcome
320 of a single model run. Frequency of image features (right) summarizes the top 5% of model
321 outcomes and the image features included in these models.

322

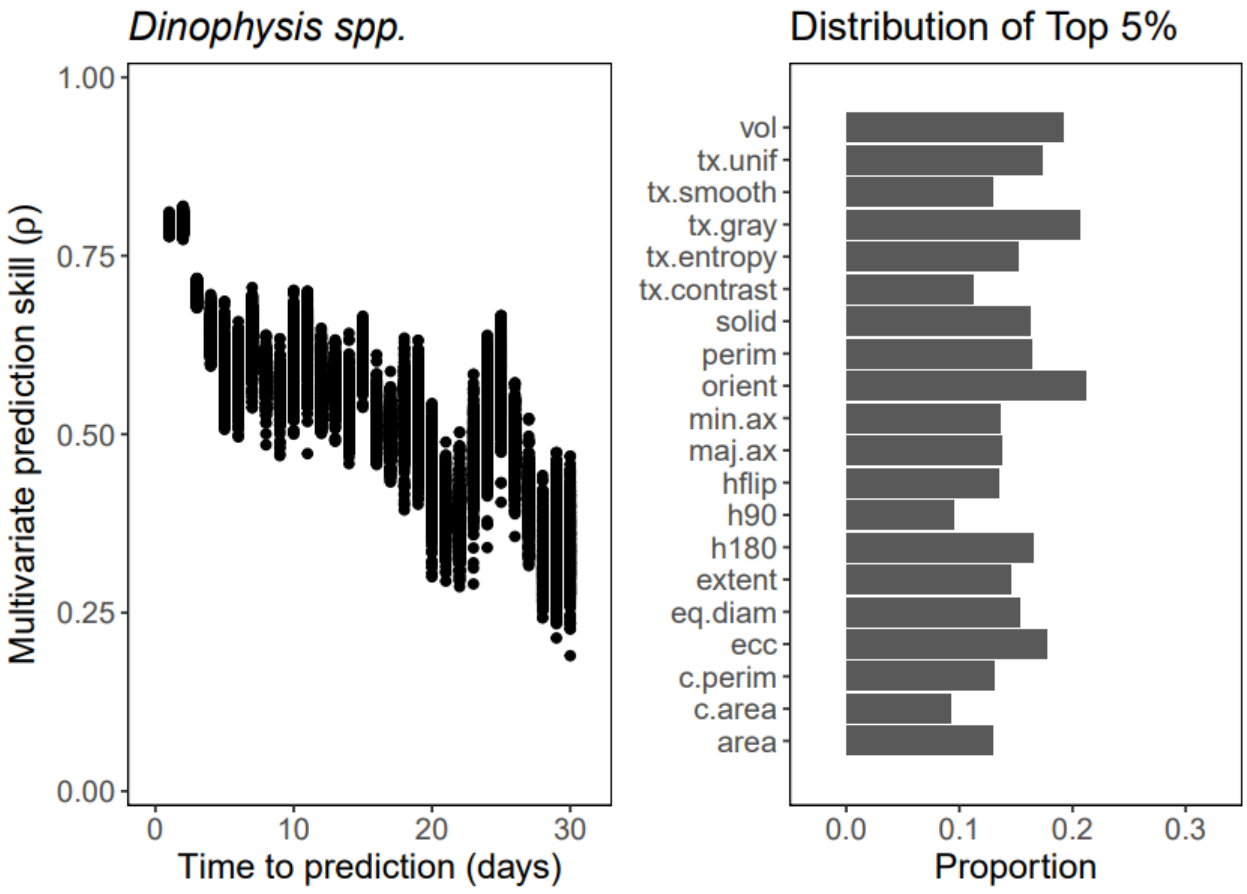

Figure 5: Multivariate prediction skill of the time series of *Dinophysis spp.* (ρ; left) over a prediction horizon of 1-30 days. Prediction skill **(ρ)** refers to the Pearson correlation coefficient between model predictions and actual observations. Model results were calculated from 1000 embeddings of phytoplankton abundance and 3 unique image features. Each point is the outcome of a single model run. Frequency of image features (right) summarizes the top 5% of model outcomes and the image features included in these models.

Environmental influence on the populations of *Pseudo-nitzschia spp.* and *Dinophysis spp.*, as measured by the cross-map prediction skill (ρ), showed variable effects across different prediction horizons. For *Pseudo-nitzschia spp.*, the prediction skill of all the environmental parameters converged with increasing library size. The strength and timescales of inferred causal influence differed across the variables. The influence of chlorophyll on *Pseudo-nitzschia spp*. had a peak at timescales around 28 days, whereas the influence of tidal height was strongest around 2

337 weeks. The time series of water temperature, pH, wind speed, and salinity showed significant and
338 consistent effects on the *Pseudo-nitzschia spp.* time series across most sub-monthly timescales.

339

340

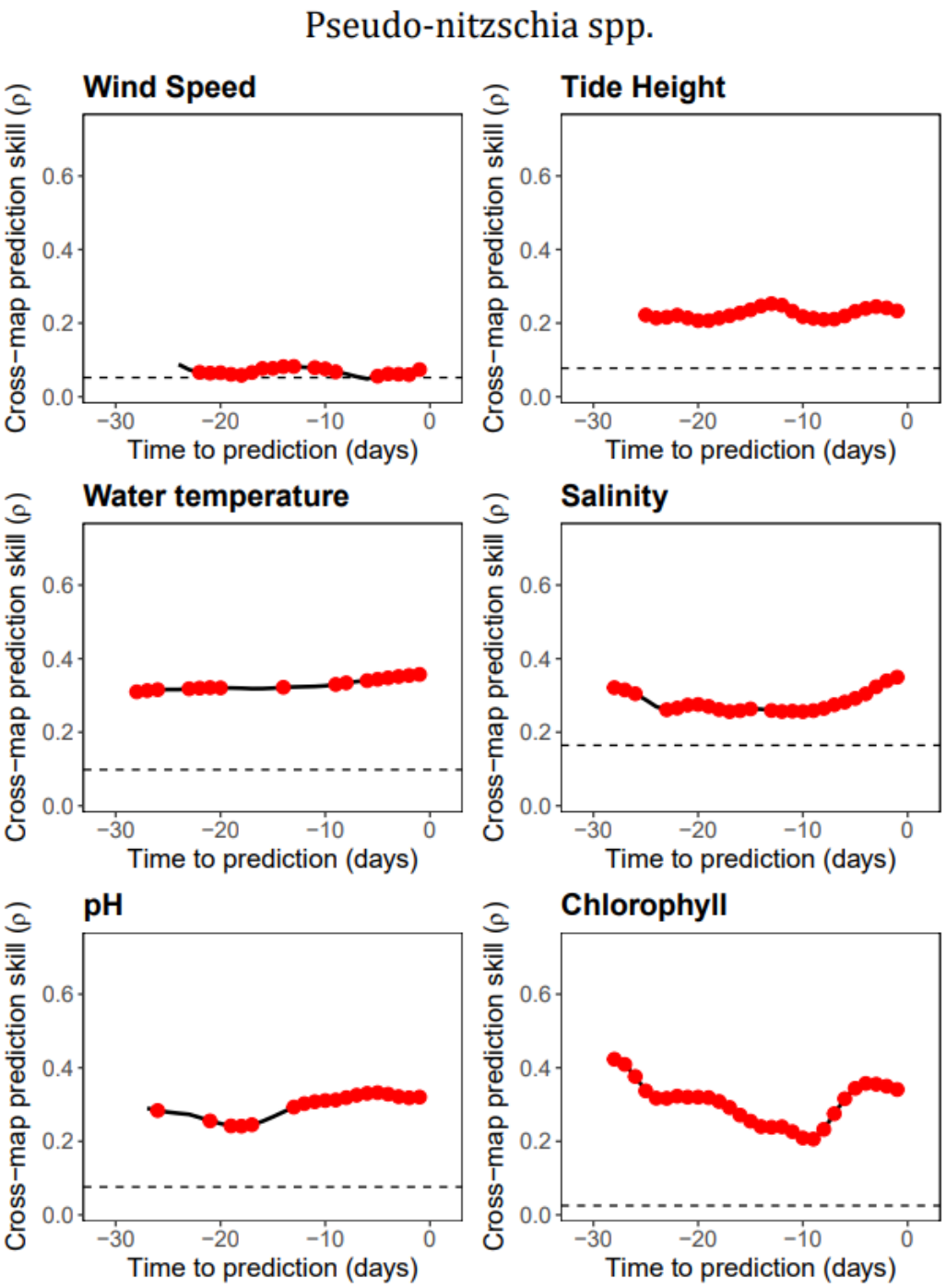

Figure 6: Influence of environmental drivers on *Pseudo-nitzschia spp.* in Narragansett Bay quantified by the cross-map prediction skill (ρ based on convergent cross mapping; see Methods). The influence was measured over a prediction horizon of 1-30 days (black line). Red points indicate which models showed convergence. The dashed line refers to the Pearson correlation coefficient between the time series of *Pseudo-nitzschia spp*. abundance and the environmental variable.

For *Dinophysis spp.*, there were more models that showed convergence across all prediction horizons. The time series of *Dinophysis spp*. was consistently affected by tide height, water temperature, and pH across all timescales. Total biomass (chlorophyll) appeared as a significant driver of *Dinophysis spp*. with peaks around 5, 14 and 27 days. The effects of salinity were consistent and stronger in the short-term (1-3 days). Predictability was higher than the Pearson correlation coefficient for most environmental variables and showed consistency, which might suggest specific mechanisms of causal influence.

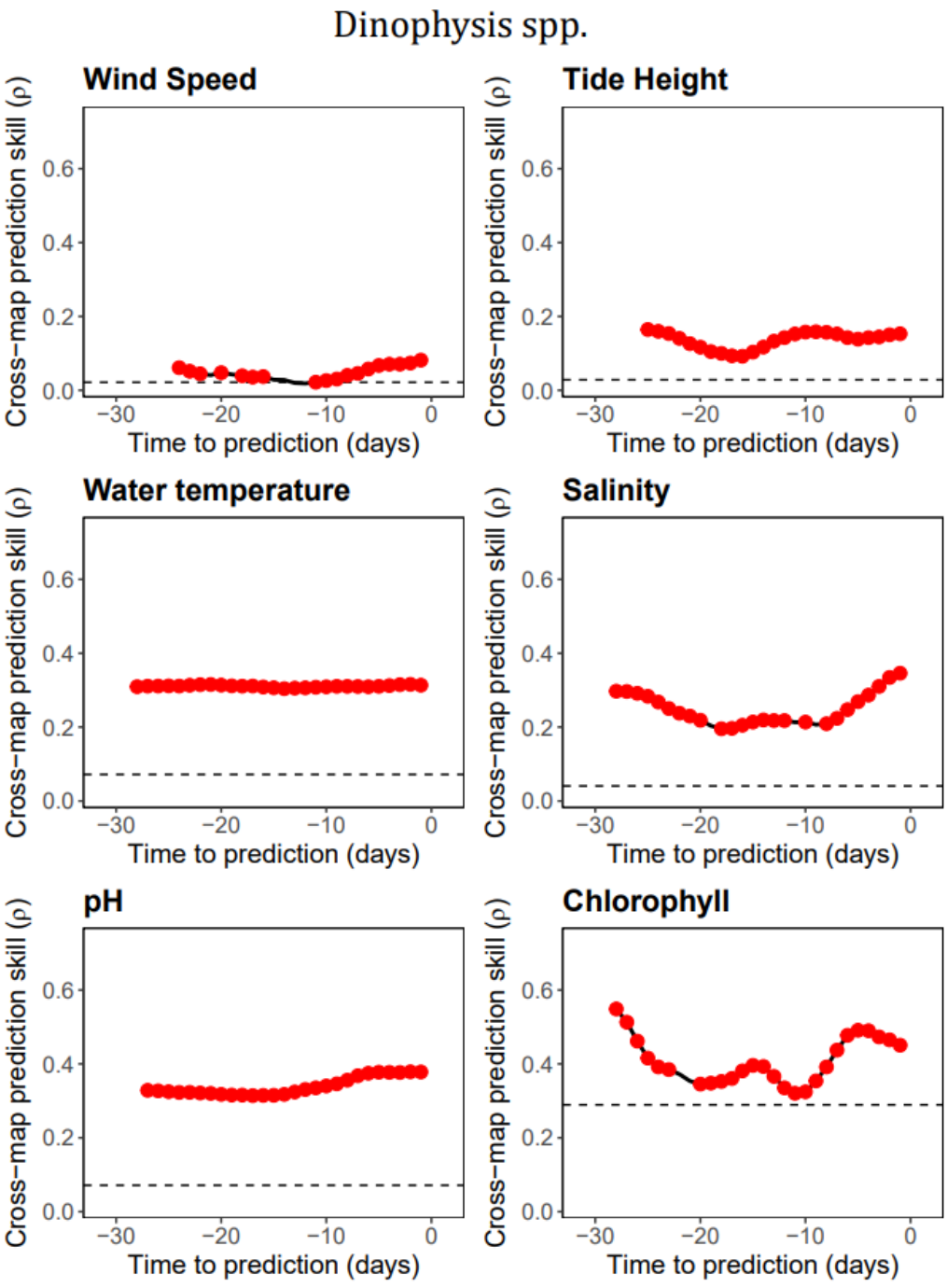

Figure 7: Influence of environmental drivers on *Dinophysis spp.* in Narragansett Bay quantified by the cross-map prediction skill (ρ based on convergent cross mapping; see Methods). The influence was measured over a prediction horizon of 1-30 days (black line). Red points indicate which models showed convergence. The dashed line refers to the Pearson correlation coefficient between the time series of *Dinophysis spp*. abundance and the environmental variable.

Discussion

Predictability of Pseudo-nitzschia spp. and Dinophysis spp.

Perturbations in phytoplankton population dynamics typically decorrelate within timescales of a month (Kuhn et al. 2019). When we tested for the inherent autocorrelation within the time series of both *Pseudo-nitzschia spp.* and *Dinophysis spp.*, we found that the autocorrelation decreased significantly within the first 10 days for *Pseudo-nitzschia spp.,* but *Dinophysis spp.* had higher autocorrelation for up to 30 days. After accounting for autocorrelation, the univariate predictability of both *Pseudo-nitzschia spp.* and *Dinophysis spp.* was low overall; however, the univariate predictability of *Pseudo-nitzschia spp.* showed some cyclical behavior. Our univariate models likely picked up on repetitive population-level mechanisms that increased or decreased abundance on sub-monthly timescales. Some examples of such mechanisms could include regular switching between periods of growth and sexual reproduction (D'Alelio et al. 2009; Annunziata et al. 2022), density-dependent interactions with parasitic protists (Berdjeb et al. 2018), or the tidal transport of productive populations from nearby sites (Shanks et al. 2014). Part of the lack of univariate predictability could be due to the presence of measurement error and stochasticity in the time series of both taxa, as well as a general lack of natural predictability for larger diatoms and dinoflagellates (Agarwal et al. 2021).

In the multivariate case, we found the predictability of both *Pseudo-nitzschia spp.* and *Dinophysis spp.* improved on timescales of greater than 1 week. Multiview embeddings have been previously shown to improve the univariate predictability of short time series (Ye and Sugihara 2016). By leveraging information stored across multiple related image features, our approach of randomly creating non-lagged embeddings could have allowed us to create better and more reliable estimates of predictive dynamics (Ma et al. 2018). The cyclical predictability of *Pseudo-nitzschia*

385 *spp.* was more prominent in the multivariate models, implicating predictable behavior on 16-day
386 and 25-day timescales. *Dinophysis spp.* was most predictable on timescales of 25 days. Due to the
387 presence of distinct timescales of predictability for both taxa, our results suggest that future
388 development of HAB models would benefit by resolving dynamics on daily and weekly
389 timescales. The identification of relevant ecological and environmental drivers of population
390 dynamics on these timescales might also aid in the development of automated monitoring and
391 early-warning systems.

392

393 *Relative contribution of IFCB image features*

394 When we evaluated the relative proportions of image features among the top multivariate
395 models, the time series of biovolume was prominently present for *Pseudo-nitzschia spp*. and
396 *Dinophysis spp.* This implies that the time series of biovolume adds considerable information to
397 the future predictability of harmful algal taxa. Biovolume estimates from IFCB images (Moberg
398 and Sosik 2012) are often used as an important marker of phytoplankton community structure and
399 function (Brosnahan et al. 2015; Oliver et al. 2021). Although image-derived biovolume estimates
400 might differ from microscopy-derived estimates (Kraft et al. 2021), cell biovolume typically varies
401 linearly with other phytoplankton functional traits (Edwards et al. 2012). Our results suggest that
402 including biovolume estimates and other high-performing image descriptors into models for
403 harmful algal taxa improves predictability beyond autocorrelation.

404 Image descriptors derived from flow cytometers have found utility in studies of
405 phytoplankton morphology (Sonnet et al. 2022), as well as for the training of different image
406 classifiers (Mosleh et al. 2012; Zheng et al. 2017). In general, "features" from an IFCB image are

all calculated from the pixels of the image and the relationships between them (see Table 2). As most features share the fundamental quantity underlying their calculations (i.e. the image itself), we expect all time series to be nonlinear approximations of one another. The relatively consistent proportions of most features in the top multivariate models indicate that the use of features themselves, and not necessarily their "character", increases the predictability of harmful algal taxa. Unless there is a particular reason to prefer one feature for another (such as biovolume for its relationship to other traits), prediction models relying on automated imaging systems would benefit from using any associated image data. Detailed information on the causal relationships between image features for *Pseudo-nitzschia spp.*, as well as the partial correlations between each image feature and our time series of image concentration, can be found in the Supplemental material.

Potential environmental drivers

To further investigate the timescales of prediction for both *Pseudo-nitzschia spp*. and *Dinophysis spp.*, we evaluated any inferred causal relationships between environmental drivers and the proxy abundance of each taxon. Consistent causal influence on either taxon would show variable but significant, effects across sub-monthly timescales. We found that both *Pseudo-nitzschia spp*. and *Dinophysis spp*. are affected by water temperatures, wind speed, tidal height, salinity, pH, and total biomass (chlorophyll). Previous studies across various regions, have hypothesized correlative relationships between harmful algal blooms and these environmental drivers (Almandoz et al. 2007; Sildever et al. 2019; Zhang et al. 2020; Lima et al. 2022). In our study, convergent model predictions with increasing library size and prediction skills that greatly exceeded the Pearson correlation coefficients between the individual time series indicate that there

are causal relationships beyond simple covariance. None of the environmental drivers we tested overlapped with the previously quantified multivariate timescales. This implies that the dynamics of both taxa in Narragansett Bay are subject to multiple context-dependent forces that interact with each other. Successful prediction models for *Pseudo-nitzschia spp*. and *Dinophysis spp.* would need to incorporate the specific local conditions under which the harmful algal blooms develop. An ideal prediction model would attempt to combine data from relevant image properties and environmental drivers for particular timescales of prediction. Different model combinations could be optimized for forecasting at certain points during the 30-day prediction horizon. Table S3 explores the outcomes of some illustrative combined models for both *Pseudo-nitzschia spp.* and *Dinophysis spp.* with a prediction horizon of 5, 10 and 15 days. Our results also indicate that there can be lags between an environmental driver and the driven harmful algal taxa. Future studies that attempt to predict the dynamics of *Pseudo-nitzschia spp.* and *Dinophysis spp.* might need to characterize the causal timescales of their predictors.

As there has been rapid deployment of automated imaging systems for the early detection of harmful algal bloom events (Campbell et al. 2010, 2013), our results suggest that there is potential to use such data sources in advanced prediction models. Monitoring programs that concurrently deploy other environmental and biogeochemical sensors might be able characterize the relevant timescales of dynamics, and consequently, predict the magnitude and spatial distribution of harmful algal events across broader regions. Although this study focuses on the population dynamics of the harmful algal bloom-causing taxa, our prediction models could also be coupled with other broad-scale ecosystem models to potentially include the impacts on higher trophic levels and human health.

Study limitations and future directions

Although we have demonstrated the potential of using automated cell imaging data in prediction models, there are several considerations involved that merit further discussion. First, as our sampling location is fixed, the influence of different water masses and a lack of spatial information can limit real-time projections of HAB abundance across entire regions. Future studies should consider the concurrent deployment of multiple different systems to accurately map and forecast spatial population patterns. Second, as *Pseudo-nitzschia spp.* is a chain-forming diatom, the use of image concentration is not a measure of the actual abundance of the taxon within the water column – there can be a variable number of cells within an image. Instead, image concentration is a measure of our ability to detect and identify the taxa. Although detection numbers are high when abundance is typically high (Figure S1), future studies might need to accurately quantify the relationship between the in-situ abundance of chain-forming organisms and their image detection. Third, the deployment and maintenance of IFCB systems may lead to some irregularities and gaps within a long-term time series. Despite multiple years of data collection, a large proportion of our daily-scale time series had to be approximated from existing observations. Our approach requires sufficient long-term coverage for the development of prediction models and future studies could evaluate alternative methods of data processing and interpolation of missing observations. Fourth, the development of harmful algal blooms likely depends on a suite of unknown environmental triggers (such as the nutrient regime, ambient light levels, etc.). The identification of specific causal mechanisms would depend on careful experimentation in laboratory studies, where confounding factors can be controlled, and additive influence can be disentangled.

Acknowledgments

This study was supported by the Rhode Island Sea Grant (Grant number: NA22OAR4170123) and NASA (Grant Supplement: NNX14AB80G). We would like to thank Heather Stoffel for the provision of environmental data at the sampling location and Audrey Ciochetto for managing the Imaging FlowCytobot data streams, instrument maintenance, image processing and databasing. We would also like to acknowledge the efforts of Jessica Carney and Virginie Sonnet for IFCB image annotations. The following students have helped maintain the IFCB over the years of operation: Kyle Turner, Ian Lew, Cassandra Alexander, Christopher Jenkins, Jessica Carney, Virginie Sonnet, and Somang Song.

References

Agarwal, V., C. C. James, C. E. Widdicombe, and A. D. Barton. 2021. Intraseasonal predictability of natural phytoplankton population dynamics. Ecol. Evol. **11**: 15720–15739. doi:10.1002/ece3.8234

Almandoz, G. O., M. E. Ferrario, G. A. Ferreyra, I. R. Schloss, J. L. Esteves, and F. E. Paparazzo. 2007. The genus Pseudo-nitzschia (Bacillariophyceae) in continental shelf waters of Argentina (Southwestern Atlantic Ocean, 38-55°S). Harmful Algae **6**: 93–103. doi:10.1016/j.hal.2006.07.003

Anderson, C. R., M. R. P. Sapiano, M. B. K. Prasad, W. Long, P. J. Tango, C. W. Brown, and R. Murtugudde. 2010. Predicting potentially toxigenic Pseudo-nitzschia blooms in the Chesapeake Bay. J. Mar. Syst. **83**: 127–140. doi:10.1016/j.jmarsys.2010.04.003

Anderson, D. M., P. Hoagland, Y. Kaoru, and A. W. White. 2000. Estimated annual economic impacts from harmful algal blooms (HABs) in the United States.

Annunziata, R., B. H. Mele, P. Marotta, and others. 2022. Trade-off between sex and growth in diatoms: Molecular mechanisms and demographic implications. Sci. Adv. **8**: 1–17. doi:10.1126/sciadv.abj9466

Ascioti, F. A., E. Beltrami, T. O. Carroll, and C. Wirick. 1993. Is there chaos in plankton dynamics? J. Plankton Res. **15**: 603–617. doi:10.1093/plankt/15.6.603

Babin, M., J. J. Cullen, C. S. Roesler, and others. 2005. New approaches and technologies for observing harmful algal blooms. Oceanography **18**: 210–227. doi:10.5670/oceanog.2005.55

Barton, A. D., A. J. Irwin, Z. V. Finkel, and C. A. Stock. 2016. Anthropogenic climate change

517 drives shift and shuffle in North Atlantic phytoplankton communities. Proc. Natl. Acad. Sci.
518 U. S. A. **113**: 2964–2969. doi:10.1073/pnas.1519080113

519 Bates, S. S., K. A. Hubbard, N. Lundholm, M. Montresor, and C. P. Leaw. 2018. Pseudo-
520 nitzschia, Nitzschia, and domoic acid: New research since 2011. Harmful Algae **79**: 3–43.
521 doi:10.1016/j.hal.2018.06.001

522 Béchard, A. 2020. Economics losses to fishery and seafood related businesses during harmful
523 algal blooms. Fish. Res. **230**: 105678. doi:10.1016/j.fishres.2020.105678

524 Berdalet, E., L. E. Fleming, R. Gowen, and others. 2016. Marine harmful algal blooms, human
525 health and wellbeing: Challenges and opportunities in the 21st century. J. Mar. Biol. Assoc.
526 United Kingdom **96**: 61–91. doi:10.1017/S0025315415001733

527 Berdjeb, L., A. Parada, D. M. Needham, and J. A. Fuhrman. 2018. Short-term dynamics and
528 interactions of marine protist communities during the spring-summer transition. ISME J. **12**:
529 1907–1917. doi:10.1038/s41396-018-0097-x

530 Blauw, A. N., E. Benincà, R. W. P. M. Laane, N. Greenwood, and J. Huisman. 2018.
531 Predictability and environmental drivers of chlorophyll fluctuations vary across different
532 time scales and regions of the North Sea. Prog. Oceanogr. **161**: 1–18.
533 doi:10.1016/j.pocean.2018.01.005

534 Brooks, B. W., J. M. Lazorchak, M. D. A. Howard, and others. 2016. Are harmful algal blooms
535 becoming the greatest inland water quality threat to public health and aquatic ecosystems?
536 Environ. Toxicol. Chem. **35**: 6–13. doi:10.1002/etc.3220

537 Brosnahan, M. L., L. Velo-Suárez, D. K. Ralston, and others. 2015. Rapid growth and concerted

sexual transitions by a bloom of the harmful dinoflagellate Alexandrium fundyense (Dinophyceae). Limnol. Oceanogr. **60**: 2059–2078. doi:10.1002/lno.10155

Brown, A. R., M. Lilley, J. Shutler, C. Lowe, Y. Artioli, R. Torres, E. Berdalet, and C. R. Tyler. 2020. Assessing risks and mitigating impacts of harmful algal blooms on mariculture and marine fisheries. Rev. Aquac. **12**: 1663–1688. doi:10.1111/raq.12403

Campbell, L., D. W. Henrichs, R. J. Olson, and H. M. Sosik. 2013. Continuous automated imaging-in-flow cytometry for detection and early warning of Karenia brevis blooms in the Gulf of Mexico. Environ. Sci. Pollut. Res. **20**: 6896–6902. doi:10.1007/s11356-012-1437-4

Campbell, L., R. J. Olson, H. M. Sosik, A. Abraham, D. W. Henrichs, C. J. Hyatt, and E. J. Buskey. 2010. First harmful dinophysis (dinophyceae, dinophysiales) bloom in the U.S. is revealeD by automated imaging flow cytometry. J. Phycol. **46**: 66–75. doi:10.1111/j.1529-8817.2009.00791.x

Carstensen, J., R. Klais, and J. E. Cloern. 2015. Phytoplankton blooms in estuarine and coastal waters: Seasonal patterns and key species. Estuar. Coast. Shelf Sci. **162**: 98–109. doi:10.1016/j.ecss.2015.05.005

Chang, C. W., M. Ushio, and C. hao Hsieh. 2017. Empirical dynamic modeling for beginners. Ecol. Res. **32**: 785–796. doi:10.1007/s11284-017-1469-9

Chavez, F. P., J. Ryan, S. E. Lluch-Cota, and C. M. Ñiquen. 2003. Climate: From anchovies to sardines and back: Multidecadal change in the Pacific Ocean. Science (80-.). **299**: 217–221. doi:10.1126/science.1075880

Cundell, A. M. 1973. Plastic materials accumulating in Narragansett Bay. Mar. Pollut. Bull. **4**:

187–188. doi:10.1016/0025-326X(73)90226-9

D'Alelio, D., A. Amato, A. Luedeking, and M. Montresor. 2009. Sexual and vegetative phases in the planktonic diatom Pseudo-nitzschia multistriata. Harmful Algae **8**: 225–232. doi:10.1016/j.hal.2008.05.004

Dalton, T., R. Thompson, and D. Jin. 2010. Mapping human dimensions in marine spatial planning and management: An example from Narragansett Bay, Rhode Island. Mar. Policy **34**: 309–319. doi:10.1016/j.marpol.2009.08.001

Dippner, J. W., L. Nguyen-Ngoc, H. Doan-Nhu, and A. Subramaniam. 2011. A model for the prediction of harmful algae blooms in the Vietnamese upwelling area. Harmful Algae **10**: 606–611. doi:10.1016/j.hal.2011.04.012

Edwards, K. F., M. K. Thomas, C. A. Klausmeier, and E. Litchman. 2012. Allometric scaling and taxonomic variation in nutrient utilization traits and maximum growth rate of phytoplankton. Limnol. Oceanogr. **57**: 554–566. doi:10.4319/lo.2012.57.2.0554

Ellen, J. S., C. A. Graff, and M. D. Ohman. 2019. Improving plankton image classification using context metadata. Limnol. Oceanogr. Methods **17**: 439–461. doi:10.1002/lom3.10324

Fleming, L. E., B. Kirkpatrick, L. C. Backer, and others. 2011. Review of Florida red tide and human health effects. Harmful Algae **10**: 224–233. doi:10.1016/j.hal.2010.08.006

Franks, P. J. S. 2018. Recent Advances in Modelling of Harmful Algal Blooms, p. 359–377. *In* Global Ecology and Oceanography of Harmful Algal Blooms.

Gobler, C. J. 2020. Climate Change and Harmful Algal Blooms: Insights and perspective. Harmful Algae **91**: 101731. doi:10.1016/j.hal.2019.101731

580 Goldberg, E. D., E. Gamble, J. J. Griffin, and M. Koide. 1977. Pollution history of Narragansett
581 Bay as recorded in its sediments. Estuar.Coastal Mar.Sci. **5**: 549–558. doi:10.1016/0302-
582 3524(77)90101-3

583 Grattan, L. M., S. Holobaugh, and J. G. Morris. 2016. Harmful algal blooms and public health.
584 Harmful Algae **57**: 2–8. doi:10.1016/j.hal.2016.05.003

585 Herndon, R. W., and E. W. Sekatau. 1997. The Right to a Name: The Narragansett People and
586 Rhode Island Officials in the Revolutionary Era. Ethnohistory **44**: 433–462.

587 Jochens, A. E., T. C. Malone, R. P. Stumpf, and others. 2010. Integrated Ocean Observing
588 System in Support of Forecasting Harmful Algal Blooms. Mar. Technol. Soc. J. **44**: 99–121.
589 doi:10.4031/MTSJ.44.6.16

590 Karlson, B., P. Andersen, L. Arneborg, and others. 2021. Harmful algal blooms and their effects
591 in coastal seas of Northern Europe. Harmful Algae **102**: 101989.
592 doi:10.1016/j.hal.2021.101989

593 Kouakou, C. R. C., and T. G. Poder. 2019. Economic impact of harmful algal blooms on human
594 health: A systematic review. J. Water Health **17**: 499–516. doi:10.2166/wh.2019.064

595 Kraft, K., J. Seppälä, H. Hällfors, and others. 2021. First Application of IFCB High-Frequency
596 Imaging-in-Flow Cytometry to Investigate Bloom-Forming Filamentous Cyanobacteria in
597 the Baltic Sea. Front. Mar. Sci. **8**: 1–17. doi:10.3389/fmars.2021.594144

598 Kuhn, A. M., S. Dutkiewicz, O. Jahn, S. Clayton, T. A. Rynearson, M. R. Mazloff, and A. D.
599 Barton. 2019. Temporal and Spatial Scales of Correlation in Marine Phytoplankton
600 Communities. J. Geophys. Res. Ocean. **124**: 9417–9438. doi:10.1029/2019JC015331

Lapucci, C., F. Maselli, G. Chini Zittelli, and others. 2022. Towards the Prediction of Favourable Conditions for the Harmful Algal Bloom Onset of Ostreopsis ovata in the Ligurian Sea Based on Satellite and Model Data. J. Mar. Sci. Eng. **10**: 461. doi:10.3390/jmse10040461

Lima, M. J., P. Relvas, and A. B. Barbosa. 2022. Variability patterns and phenology of harmful phytoplankton blooms off southern Portugal: Looking for region-specific environmental drivers and predictors. Harmful Algae **116**: 102254. doi:10.1016/j.hal.2022.102254

Ma, H., S. Leng, K. Aihara, W. Lin, and L. Cheni. 2018. Randomly distributed embedding making short-term high-dimensional data predictable. Proc. Natl. Acad. Sci. U. S. A. **115**: E9994–E10002. doi:10.1073/pnas.1802987115

McLeod, A.I. 2022. Kendall: Kendall Rank Correlation and Mann-Kendall Trend Test. R package version 2.2.1. https://CRAN.R-project.org/package=Kendall

Moberg, E. A., and H. M. Sosik. 2012. Distance maps to estimate cell volume from two-dimensional plankton images. Limnol. Oceanogr. Methods **10**: 278–288. doi:10.4319/lom.2012.10.278

Moritz S, Bartz-Beielstein T. 2017. “imputeTS: Time Series Missing Value Imputation in R.” The R Journal **9**(1), 207-218. doi: 10.32614/RJ-2017-009

Mosleh, M. A. A., H. Manssor, S. Malek, P. Milow, and A. Salleh. 2012. A preliminary study on automated freshwater algae recognition and classification system. BMC Bioinformatics **13 Suppl 1**. doi:10.1186/1471-2105-13-s17-s25

Nixon, S. W., and R. W. Fulweiler. 2012. Ecological footprints and shadows in an urban estuary, Narragansett Bay, RI (USA). Reg. Environ. Chang. **12**: 381–394. doi:10.1007/s10113-011-

0221-1

Oliver, H., W. G. Zhang, W. O. Smith, and others. 2021. Diatom Hotspots Driven by Western Boundary Current Instability. Geophys. Res. Lett. **48**: 1–10. doi:10.1029/2020GL091943

Olson, R. J., and H. M. Sosik. 2007. A submersible imaging-in-flow instrument to analyze nano- and microplankton: Imaging FlowCytobot. Limnol. Oceanogr. Methods **5**: 195–203. doi:10.4319/lom.2007.5.195

Orenstein, E. C., K. M. Kenitz, P. L. D. Roberts, P. J. S. Franks, J. S. Jaffe, and A. D. Barton. 2020. Semi- and fully supervised quantification techniques to improve population estimates from machine classifiers. Limnol. Oceanogr. Methods **18**: 739–753. doi:10.1002/lom3.10399

Park, T. G., W. A. Lim, Y. T. Park, C. K. Lee, and H. J. Jeong. 2013. Economic impact, management and mitigation of red tides in Korea. Harmful Algae **30**: S131–S143. doi:10.1016/j.hal.2013.10.012

Park, Joseph, C. Smith, G. Sugihara and E. Deyle. 2022. rEDM: Empirical Dynamic Modeling ('EDM'). R package version 1.13.0. https://CRAN.R-project.org/package=rEDM

Perretti, C. T., S. B. Munch, and G. Sugihara. 2013. Model-free forecasting outperforms the correct mechanistic model for simulated and experimental data. Proc. Natl. Acad. Sci. U. S. A. **110**: 5253–5257. doi:10.1073/pnas.1216076110

Pilson, M. E. Q. 1985. On the residence time of water in Narragansett Bay. Estuaries **8**: 2–14. doi:10.2307/1352116

R Core Team. 2021. R: A language and environment for statistical computing. R Foundation for

643 Statistical Computing, Vienna, Austria. URL https://www.R-project.org/.

644 Ralston, D. K., and S. K. Moore. 2020. Modeling harmful algal blooms in a changing climate.
645 Harmful Algae **91**: 1–29. doi:10.1016/j.hal.2019.101729

646 Saberski, E., A. K. Bock, R. Goodridge, V. Agarwal, T. Lorimer, S. A. Rifkin, and G. Sugihara.
647 2021. Networks of causal linkage between eigenmodes characterize behavioral dynamics of
648 caenorhabditis elegans. PLoS Comput. Biol. **17**: 1–15. doi:10.1371/journal.pcbi.1009329

649 Sakamoto, S., W. A. Lim, D. Lu, X. Dai, T. Orlova, and M. Iwataki. 2021. Harmful algal blooms
650 and associated fisheries damage in East Asia: Current status and trends in China, Japan,
651 Korea and Russia. Harmful Algae **102**: 101787. doi:10.1016/j.hal.2020.101787

652 Scavia, D., J. C. Field, D. F. Boesch, and others. 2002. Climate change impacts on U.S. Coastal
653 and Marine Ecosystems. Estuaries **25**: 149–164. doi:10.1007/BF02691304

654 Shanks, A. L., S. G. Morgan, J. MacMahan, A. J. H. M. Reniers, M. Reniers, J. Brown, A.
655 Fujimura, and C. Griesemer. 2014. Onshore transport of plankton by internal tides and
656 upwelling-relaxation events. Mar. Ecol. Prog. Ser. **502**: 39–51. doi:10.3354/meps10717

657 Sildever, S., Y. Kawakami, N. Kanno, H. Kasai, A. Shiomoto, S. Katakura, and S. Nagai. 2019.
658 Toxic HAB species from the Sea of Okhotsk detected by a metagenetic approach,
659 seasonality and environmental drivers. Harmful Algae **87**: 101631.
660 doi:10.1016/j.hal.2019.101631

661 Smayda, T. J. 1998. Patterns of variability characterizing marine phytoplankton, with examples
662 from Narragansett Bay. ICES J. Mar. Sci. **55**: 562–573. doi:10.1006/jmsc.1998.0385

663 Smith, R. B., B. Bass, D. Sawyer, D. Depew, and S. B. Watson. 2019. Estimating the economic

costs of algal blooms in the Canadian Lake Erie Basin. Harmful Algae **87**: 101624. doi:10.1016/j.hal.2019.101624

Sonnet, V., L. Guidi, C. B. Mouw, G. Puggioni, and S. D. Ayata. 2022. Length, width, shape regularity, and chain structure: time series analysis of phytoplankton morphology from imagery. Limnol. Oceanogr. **67**: 1850–1864. doi:10.1002/lno.12171

Sosik, H. M., and R. J. Olson. 2007. Automated taxonomic classification of phytoplankton sampled with imaging-in-flow cytometry. Limnol. Oceanogr. Methods **5**: 204–216. doi:10.4319/lom.2007.5.204

Sterling, A. R., R. D. Kirk, M. J. Bertin, and others. 2022. Emerging harmful algal blooms caused by distinct seasonal assemblages of a toxic diatom. Limnol. Oceanogr. 0–1. doi:10.1002/lno.12189

Sugihara, G., and R. M. May. 1990. Nonlinear forecasting as a way of distinguishing chaos from measurement error in time series. Nature **344**: 24–26.

Sugihara, G., R. May, H. Ye, C. H. Hsieh, E. Deyle, M. Fogarty, and S. Munch. 2012. Detecting causality in complex ecosystems. Science (80-.). **338**: 496–500. doi:10.1126/science.1227079

Wickham, H. 2016. ggplot2: Elegant Graphics for Data Analysis. Springer-Verlag New York.

Wilke, Claus O. 2020. cowplot: Streamlined Plot Theme and Plot Annotations for 'ggplot2'.

Xiao, X., S. Agustí, Y. Pan, Y. Yu, K. Li, J. Wu, and C. M. Duarte. 2019. Warming Amplifies the Frequency of Harmful Algal Blooms with Eutrophication in Chinese Coastal Waters. Environ. Sci. Technol. **53**: 13031–13041. doi:10.1021/acs.est.9b03726

Ye, H., and G. Sugihara. 2016. Information leverage in interconnected ecosystems: Overcoming the curse of dimensionality. Science (80-.). **353**: 922–925. doi:10.1126/science.aag0863

Zhang, Y., J. Z. Su, Y. P. Su, H. Lin, Y. C. Xu, B. P. Barathan, W. N. Zheng, and K. G. Schulz. 2020. Spatial distribution of phytoplankton community composition and their correlations with environmental drivers in taiwan strait of Southeast China. Diversity **12**: 1–15. doi:10.3390/d12110433

Zheng, H., R. Wang, Z. Yu, N. Wang, Z. Gu, and B. Zheng. 2017. Automatic plankton image classification combining multiple view features via multiple kernel learning. BMC Bioinformatics **18**: 1–18. doi:10.1186/s12859-017-1954-8

Figure Captions

Figure 1: Time series of 2 harmful algal bloom-forming taxa in Narragansett Bay, Rhode Island (left column) and their associated autocorrelation functions (ACF; right column). Relative abundance is estimated from the number of unique images taken by the IFCB and classified as (a) *Pseudo-nitzschia spp.* and (c) *Dinophysis spp.* Autocorrelation decreases with time and varies depending on the dynamics of each specific taxon.

Figure 2: Univariate prediction skill **($\Delta\rho$)** of the time series of (a) *Pseudo-nitzschia spp.* and (b) *Dinophysis spp.* over a prediction horizon of 1-30 days. Model predictions (ρ_{model}) were calculated from 200 random libraries of 250 days each and the results were reported as an arithmetic mean with 95% confidence intervals ($\pm 1.96 \times S.E.$). $\Delta\rho$ was calculated by subtracting the autocorrelation coefficient at each prediction horizon.

Figure 3: Multivariate prediction skill of the time series of *Pseudo-nitzschia spp.* (left column) and *Dinophysis spp.* (right column) over a prediction horizon of 1-30 days. (a) and (c) report prediction skill **($\Delta\rho$)** calculated by subtracting the autocorrelation coefficient at each prediction horizon, (b) and (d) report prediction error as the root-mean-squared-error (RMSE), (e) and (f) report prediction error as the mean-absolute-error (MAE). Model results were calculated from 500 embeddings of phytoplankton abundance and 3 unique image features. The results were reported as an arithmetic mean with 95% confidence intervals ($\pm 1.96 \times S.E.$).

Figure 4: Multivariate prediction skill of the time series of *Pseudo-nitzschia spp.* (ρ; left) over a prediction horizon of 1-30 days. Prediction skill **(ρ)** refers to the Pearson correlation coefficient between model predictions and actual observations. Model results were calculated from 1000 embeddings of phytoplankton abundance and 3 unique image features. Each point is the outcome of a single model run. Frequency of image features (right) summarizes the top 5% of model outcomes and the image features included in these models.

Figure 5: Multivariate prediction skill of the time series of *Dinophysis spp.* (ρ; left) over a prediction horizon of 1-30 days. Prediction skill **(ρ)** refers to the Pearson correlation coefficient between model predictions and actual observations. Model results were calculated from 1000 embeddings of phytoplankton abundance and 3 unique image features. Each point is the outcome of a single model run. Frequency of image features (right) summarizes the top 5% of model outcomes and the image features included in these models.

Figure 6: Influence of environmental drivers on *Pseudo-nitzschia spp.* in Narragansett Bay quantified by the cross-map prediction skill (ρ based on convergent cross mapping; see Methods). The influence was measured over a prediction horizon of 1-30 days (black line). Red points

indicate which models showed convergence. The dashed line refers to the Pearson correlation coefficient between the time series of *Pseudo-nitzschia spp*. abundance and the environmental variable.

Figure 7: Influence of environmental drivers on *Dinophysis spp.* in Narragansett Bay quantified by the cross-map prediction skill (ρ based on convergent cross mapping; see Methods). The influence was measured over a prediction horizon of 1-30 days (black line). Red points indicate which models showed convergence. The dashed line refers to the Pearson correlation coefficient between the time series of *Dinophysis spp*. abundance and the environmental variable.

749 **Supplementary material**

750

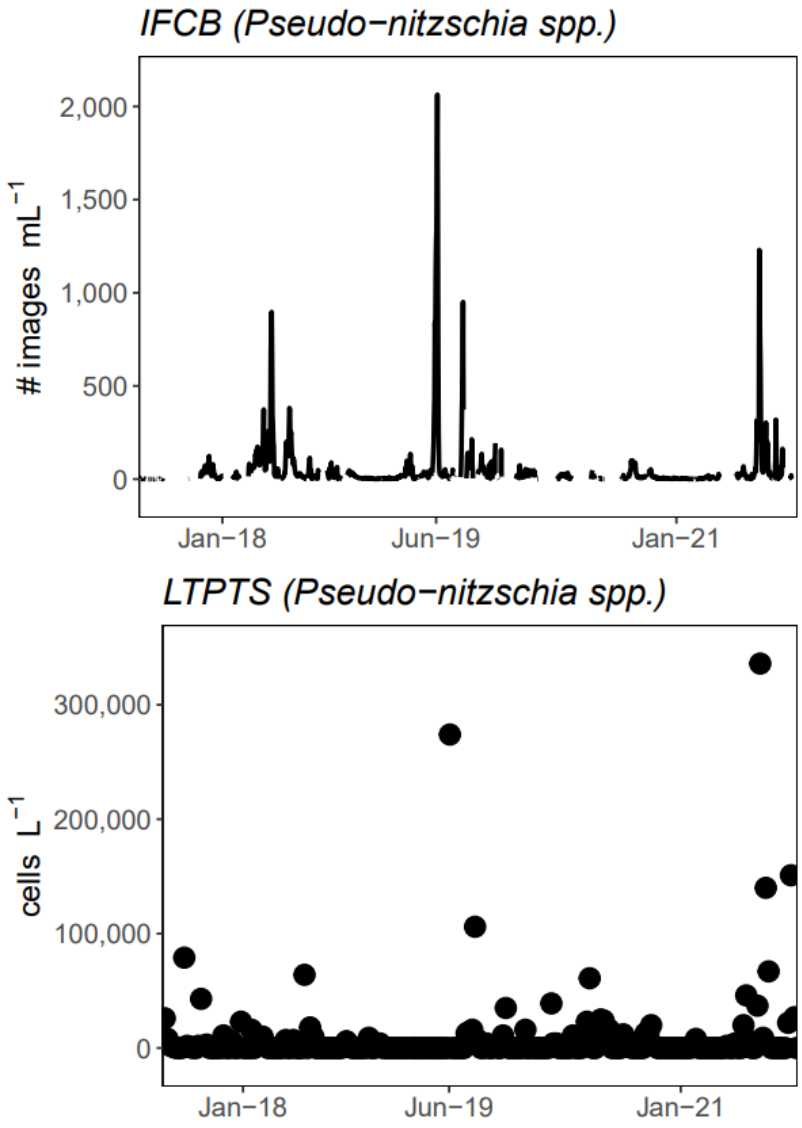

751

752 **Figure S1:** Time series of *Pseudo-nitzschia spp.* in Narragansett Bay, Rhode Island. Top panel:
753 Relative abundance as estimated from the average number of unique images taken by the IFCB
754 and reported as an image concentration. Bottom panel: Weekly cell counts of *Pseudo-nitzschia*
755 *spp.* conducted at the Narragansett Bay Long-Term Plankton Time Series
756 (https://web.uri.edu/gso/research/plankton/).
757

758

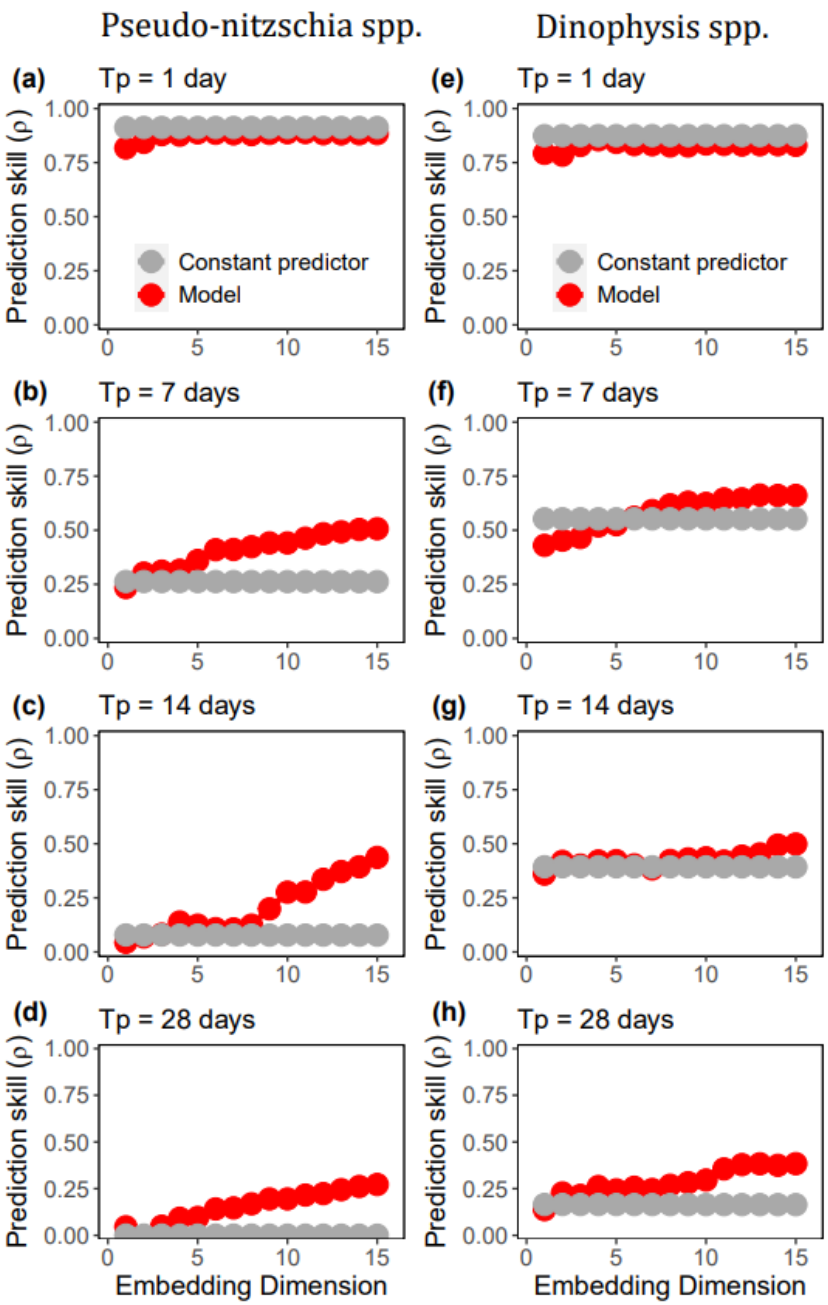

759

760 **Figure S2:** Univariate prediction skill (ρ) varies with the choice of embedding dimension and the
761 prediction horizon. Red points indicate the actual model and grey points indicate the
762 autocorrelation coefficient (i.e. constant predictor). The left column shows the results for *Pseudo-*
763 *nitzschia spp.* models run with prediction horizons of (a) 1 day (b) 7 days (c) 14 days and (d) 28
764 days. The right column similarly reports results for *Dinophysis spp.* models run with prediction
765 horizons of (e) 1 day (f) 7 days (g) 14 days and (h) 28 days.

766

An advanced test for causality is given in [1], where they provide a generalized correlation coefficient, $GMC(Y|X)$, via the Nadaraya-Watson nonparametric Kernel regression

$$Y = g(X) = \mathrm{E}[Y|X] + \epsilon$$

where $g(X)$ is a non-parametric, unspecified (non-linear) function. Some of the salient features of this methodology are

- It allows us to measure how differences or changes in X affect the differences or changes in Y in a non-linear way. Nonetheless, this measurement is normalized to be a number between -1 and 1, allowing us to make a comparison between the generalized correlation coefficients of two pairs of time series. Keeping the notation in the original paper, we will write that $R^{\star}(i,j) = r^{\star}\left(X_i \middle| X_j\right)$ is the generalized correlation coefficient of the factor X_i given the factor X_j.

- It is not a symmetric measurement. This is obvious from the definition as the conditional expectations satisfy that $E[Y|X] \neq E[X|Y]$. Moreover, precisely because of this definition, GMC establishes a framework where causality can be analyzed. This becomes particularly important because it allow us to see whether any of the features of our dataset has a direct causality relation to the feature that we want to forecast, which is "number". Furthermore, the author establishes a generalization of Granger-Causality where if $|R^{\star}(i,j)| < |R^{\star}(j,i)|$ then the data suggests that $X_i \to X_j$. In other words, the factor X_i is the cause and the factor X_j becomes the effect.

- It is a nonlinear, nonparametric method. This means that, contrary to the common Pearson correlation coefficient, two quantities X, Y are independent if and only if $GMC(Y|X) = GMC(X|Y) = 0$. Also, as with any nonparametric method, we get the advantage of not biasing our estimates by stipulating the form of the relationship between the variables but this comes at a great computational expense, where even in a modest data set as ours it can take a lot of time to compute it.

To compute the GMC, we used the library "*generalCorr*" in R for all the pairs of factors. The obtained results can be found in Table 1 in the Appendix. It is also important to point out that in this table, the row variable x_i is the "effect" while the column variable x_j is the predictor or the "cause." Thus, if we want to see if a variable is a good predictor or "cause" (individually) for the variable "number" then we need to look at the first row.

Notice that all the factors have a generalized partial correlation between 0.26 and 0.39, in absolute value, with "number", meaning that they are not good individual predictors for this variable and there is a very weak causal relationship. To make sure we also computed the (normal) linear partial correlation coefficients, described in Table 2.

This analysis shows that no individual factor can help us in increasing our predictability and, moreover, since uniformly across the table $|R^{\star}(number|factor)| < |R^{\star}(factor|number)|$ for any factor, the data suggests that the variable we want to predict is the driver of the whole data set, as expected. However, based on the results of our methodology, we can conclude that there are different subsets of factors which, as a cluster, can actually help us understand better the behavior of the algae.

Finally, let us point out that as expected, almost all of the features are considered to be a function of another factor. This make sense as all the features are measured through a transformation of the information provided from the same picture. The only feature where we do not have a clear dependance or causality is our main response variable "number", making our methodology become more relevant as any improvement in the predictability of the algae becomes of critical importance.

References:

[1] Vinod, H. D. (2017). Generalized correlation and kernel causality with applications in development economics. Communications in Statistics-Simulation and Computation, 46(6):4513–4534.

Table 1: The matrix of Generalized correlation (for *Pseudo-nitzschia spp.*).

	number	area	vol	c.area	c.perim	ecc	eq.diam	extent	h180	h90	hflip	maj.ax	min.ax	perim	solid	tx.contrast	tx.gray	tx.entropy	tx.smooth	tx.unif	orient
number	1	0.322	0.3	0.312	0.339	0.344	0.351	0.375	0.278	0.277	0.267	0.332	0.38	0.331	0.372	0.381	0.368	0.392	0.355	0.32	-0.33
area	0.816	1	0.99	0.999	0.994	0.981	0.996	0.984	0.963	0.977	0.941	0.993	0.995	0.989	0.985	0.98	0.974	0.985	0.974	0.951	0.243
vol	0.786	0.99	1	0.986	0.972	0.948	0.976	0.953	0.933	0.948	0.909	0.969	0.975	0.964	0.955	0.949	0.942	0.955	0.942	0.92	0.139
c.area	0.817	0.999	0.985	1	0.996	0.982	0.996	0.984	0.967	0.977	0.949	0.994	0.995	0.993	0.985	0.983	0.976	0.986	0.977	0.954	0.283
c.perim	0.833	0.995	0.975	0.996	1	0.995	0.999	0.993	0.974	0.986	0.956	0.999	0.997	0.997	0.995	0.993	0.988	0.996	0.988	0.973	0.345
ecc	0.843	0.983	0.956	0.985	0.995	1	0.993	0.994	0.97	0.99	0.951	0.996	0.989	0.993	0.995	0.996	0.991	0.997	0.99	0.974	0.348
eq.diam	0.832	0.997	0.979	0.997	0.999	0.994	1	0.994	0.972	0.984	0.951	0.998	0.998	0.995	0.996	0.993	0.987	0.995	0.987	0.97	0.335
extent	0.84	0.986	0.965	0.985	0.993	0.994	0.994	1	0.965	0.981	0.943	0.993	0.992	0.987	0.997	0.992	0.987	0.995	0.985	0.97	0.243
h180	0.819	0.954	0.939	0.961	0.966	0.961	0.963	0.952	1	0.947	0.963	0.963	0.961	0.967	0.957	0.959	0.954	0.963	0.953	0.933	0.227
h90	0.837	0.973	0.948	0.974	0.982	0.988	0.979	0.978	0.952	1	0.929	0.988	0.971	0.978	0.977	0.976	0.97	0.977	0.97	0.96	0.311
hflip	0.769	0.933	0.914	0.942	0.945	0.94	0.94	0.93	0.961	0.922	1	0.941	0.939	0.949	0.93	0.945	0.937	0.944	0.942	0.929	0.347
maj.ax	0.836	0.994	0.973	0.995	0.999	0.996	0.998	0.994	0.972	0.991	0.952	1	0.995	0.996	0.995	0.993	0.987	0.995	0.987	0.972	0.344
min.ax	0.827	0.996	0.981	0.996	0.997	0.989	0.998	0.992	0.971	0.976	0.951	0.995	1	0.993	0.994	0.99	0.985	0.993	0.985	0.968	0.324
perim	0.83	0.989	0.964	0.993	0.997	0.992	0.994	0.988	0.971	0.981	0.957	0.995	0.991	1	0.988	0.991	0.985	0.992	0.985	0.973	0.391
solid	0.841	0.988	0.967	0.987	0.996	0.996	0.996	0.998	0.969	0.982	0.947	0.995	0.995	0.99	1	0.995	0.99	0.998	0.989	0.972	0.305
tx.contrast	0.835	0.982	0.956	0.984	0.993	0.995	0.992	0.991	0.967	0.98	0.953	0.992	0.99	0.991	0.993	1	0.989	0.997	0.998	0.968	0.364
tx.gray	0.811	0.978	0.956	0.979	0.988	0.989	0.987	0.987	0.967	0.974	0.951	0.987	0.985	0.986	0.989	0.99	1	0.989	0.985	0.972	0.348
tx.entropy	0.841	0.986	0.961	0.987	0.996	0.997	0.995	0.995	0.971	0.981	0.951	0.995	0.993	0.992	0.997	0.997	0.989	1	0.993	0.964	0.333
tx.smooth	0.827	0.973	0.945	0.976	0.984	0.987	0.983	0.982	0.956	0.971	0.947	0.983	0.98	0.983	0.984	0.998	0.982	0.99	1	0.957	0.382
tx.unif	0.77	0.96	0.944	0.961	0.969	0.97	0.969	0.969	0.951	0.963	0.94	0.968	0.967	0.968	0.97	0.964	0.971	0.963	0.955	1	0.175
orient	0	0.726	0.109	0.74	0.739	0.36	0.753	0.754	0.11	0.31	0.73	0.75	0.55	0.429	0.172	0.753	0.732	0.326	0.721	0.105	1

Table 2: The vector of (linear) partial correlation between all the predictors and the variable “number”.

number	area	vol	c.area	c.perim	ecc	eq.diam	extent	h180	h90	hflip	maj.ax	min.ax	perim	solid	tx.contrast	tx.gray	tx.entropy	tx.smooth	tx.unif	orient
1	-0.05	0.09	0.09	0.04	-0.01	-0.22	0.03	0.07	0.07	-0.17	0.10	0.20	0.13	0.25	-0.33	0.08	0.07	0.33	0.05	0.22

Table 3: Outcomes of multivariate models where both image features and environmental variables are combined (i.e. E = 4 with 2 image-based and 2 environmental predictors). 100 random combinations were tested for each prediction horizon (5,10 and 15 days) and the models with the highest $\Delta\rho$ are reported below.

Taxa	**Time to prediction (days)**	**Predictor 1**	**Predictor 2**	**Predictor 3**	**Predictor 4**	$\boldsymbol{\rho}$	$\boldsymbol{\Delta\rho}$
Pseudo-nitzschia spp.	5	eq.diam	ecc	water temperature	salinity	0.74	0.32
Pseudo-nitzschia spp.	10	eq.diam	extent	chlorophyll	water temperature	0.80	0.67
Pseudo-nitzschia spp.	15	solidity	c.perim	pH	water temperature	0.74	0.66
Dinophysis spp.	5	h90	tx.unif	water temperature	salinity	0.76	0.15
Dinophysis spp.	10	area	tx.gray	pH	water temperature	0.80	0.37
Dinophysis spp.	15	tx.unif	extent	pH	water temperature	0.79	0.42